Tomographic Analysis of Ionosphere and Plasmasphere

AOSWA 2016, Jeju Island, Korea

By
Yong Ha Kim, Nicholas Ssessanga, Eunsol Kim and Se-Heon Jeong
Chungnam National University
Dept. of Astronomy and Space Science
Daejeon, South Korea

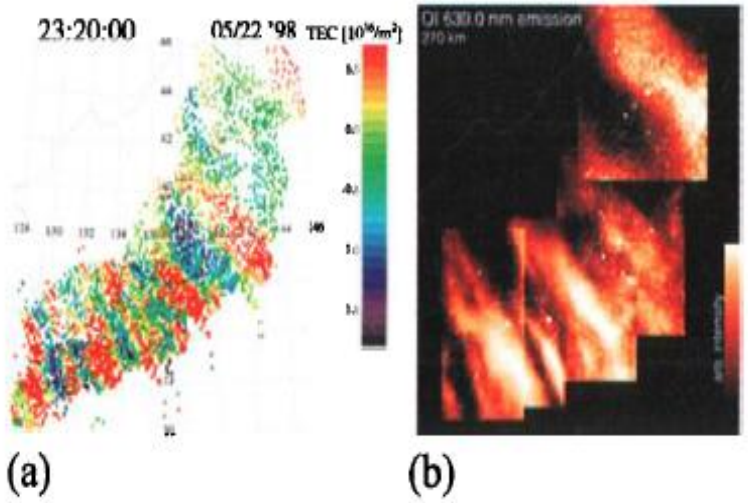

Figure 2. Two-dimensional distribution of total electron content at 23:20:00 (a) and 630nm band airglow between 23:17:34 and 23:21:39 (b) on May 22, 1998 (JST).

roduct

hy has bee

3-D struct

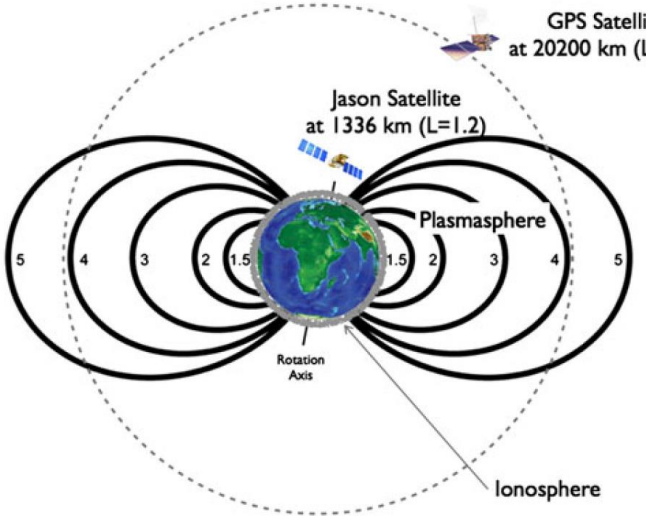

(Lee et al., 2013)

asmasphere have been probed

content (TEC) data between GPS receivers and satellites.

- Sufficient TEC databases are available in Japan for ionospheric tomography.
- Plasmaspheric TEC (pTEC) data have been accumulated by Jason-1 satellite.

http://seg-eb.nict.go.jp/Saito et al. 2001

1. Ionospheric Tomography

1. Ionospheric Tomography

- A time dependent computerized ionospheric tomography (CIT) technique is used to solve the 3-dimensional inverse problem.

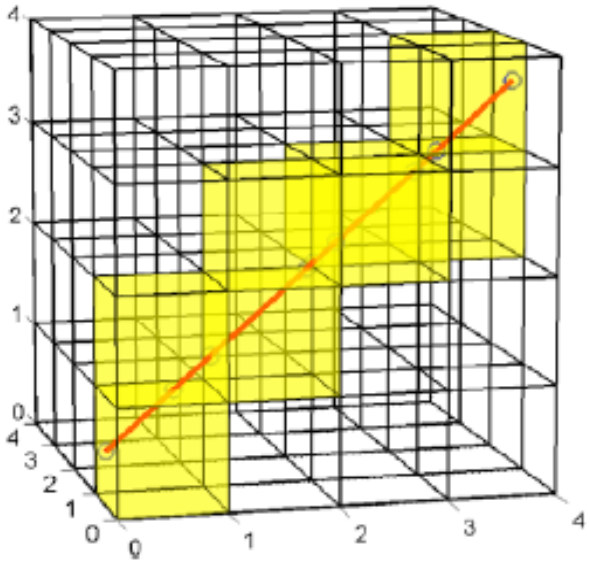

Voxels:
Latitude: 31° N – 45 ° N / 0.5 °
Longitude: 129.5 ° N – 145° N / 0.5 °
Altitude: 100 – 2000 km

we setup an SLE

$$\mathbf{AX = M(STEC) + E}$$

Design matrix

Required unknown (Electron density)

Associated error vector

Medium Scale Traveling Ionospheric Disturbances (MSTID)

- Japan has a GPS Earth Observation Network (GEONET) of more than 1000 receivers (with average distance between two neighboring points being 25-30 km).
- By taking advantage of this dense GPS network, a good spatial and temporal resolution can be obtained in vertical and horizontal

(Preliminary work was presented by Ssessanga et al., 2015)

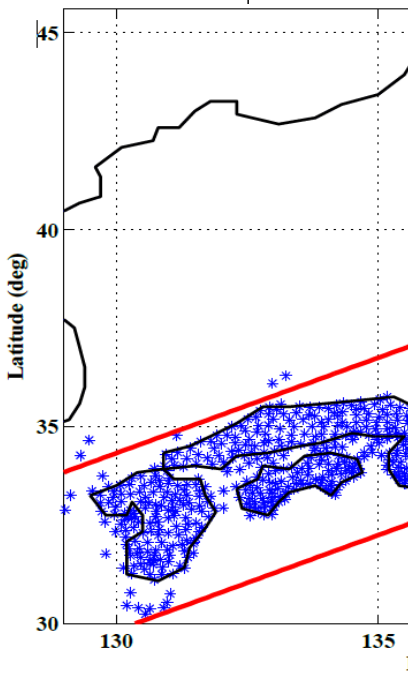

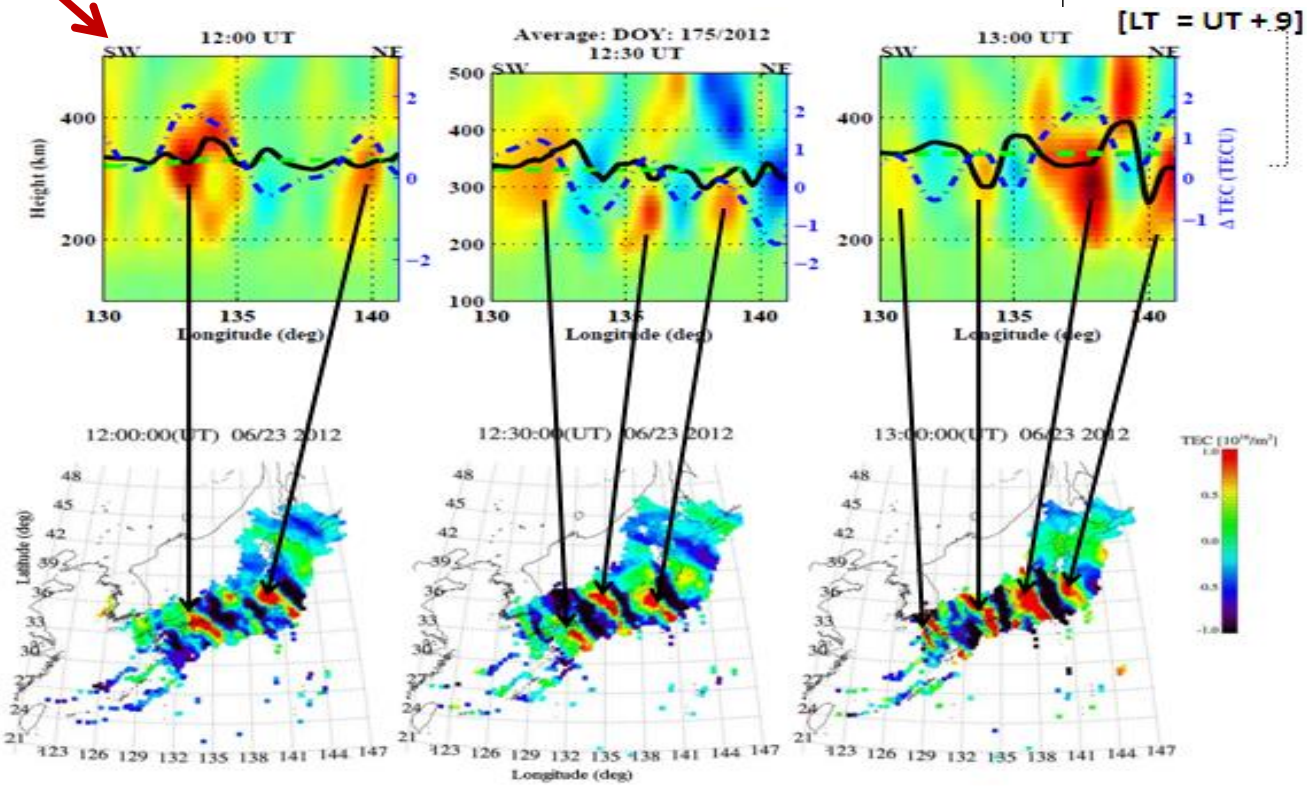

To solve the inverse problem we use the MART (Multiplicative Algebraic Reconstruction Technique)

$$x_j^{k+1} = x_j^k * \left(\frac{m_i}{\langle \boldsymbol{A}^i, \boldsymbol{x}^k \rangle} \right)^{\frac{\lambda_k A_j^i}{A_{\max}}} , \quad j = 1, \ldots, N .$$

$A_{\max}$ is the maximum path-pixel intersection length in the grid.

- $\boldsymbol{\lambda}_k$ is the relaxation parameter and controls the convergence of the algorithm.
- Since the SLE is underdetermined, we incorporate a prior information (initial guess) through the use of **local time dependent Empirical orthogonal functions (EOFs)** derived from International Reference Ionosphere (IRI-2016) model.

Algorithm validation

- We validate CIT by comparing reconstructions with
  - Manually scaled ionosonde peak electron densities (NmF2)
  - Occultation profiles from COSMIC data
  - VTEC perturbation component from NICT (ΔTEC).

Ionosonde validation

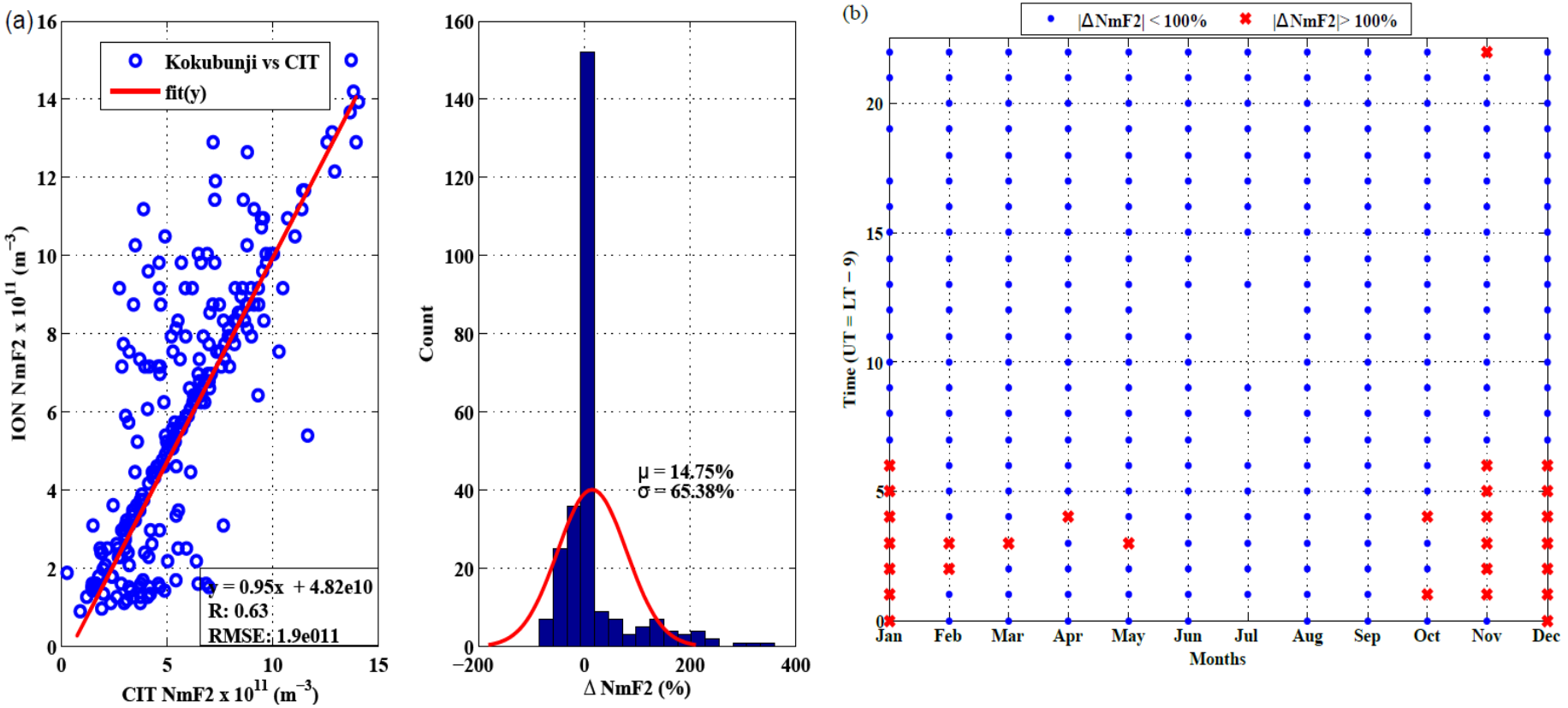

- In (b) the red data points are concentrated within day-time (06:00 UT≥ Time ≥ 00:00 UT), and during the months from November to January (winter).
- Because our CIT algorithm was fine-tuned to observation of a night-time phenomenon (MSTIDs) that mainly occurs during summer period, the change in time and season could highly deteriorate the convergence of the algorithm and thus the fidelity.

Occultation traces (COSMIC)

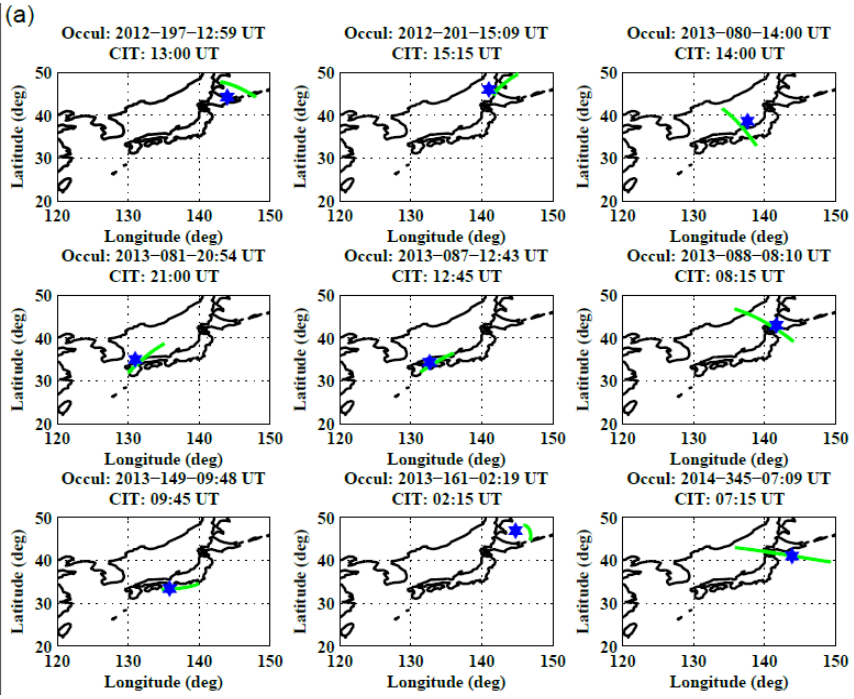

Profiles

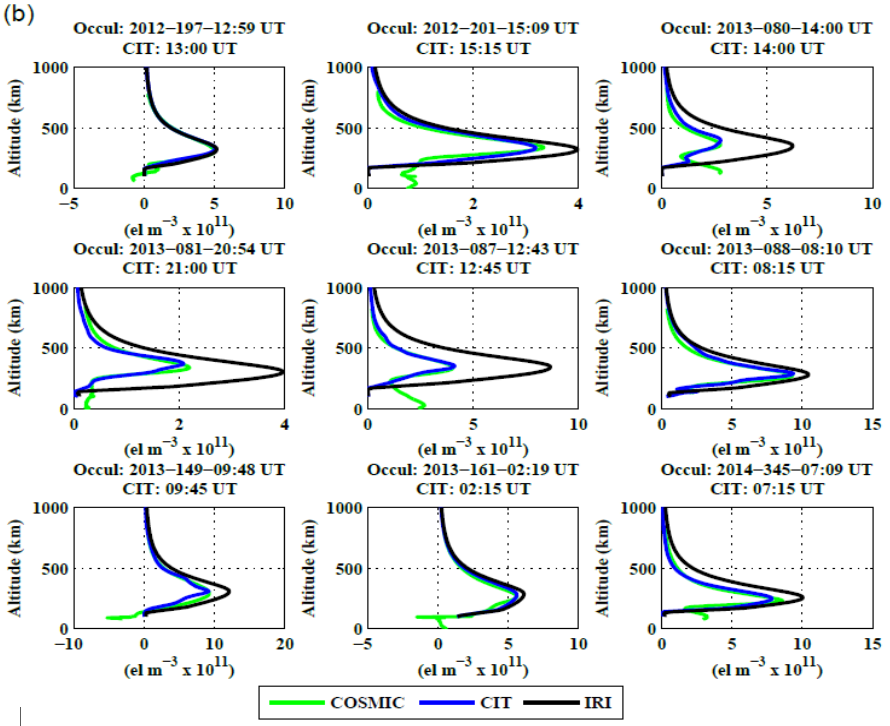

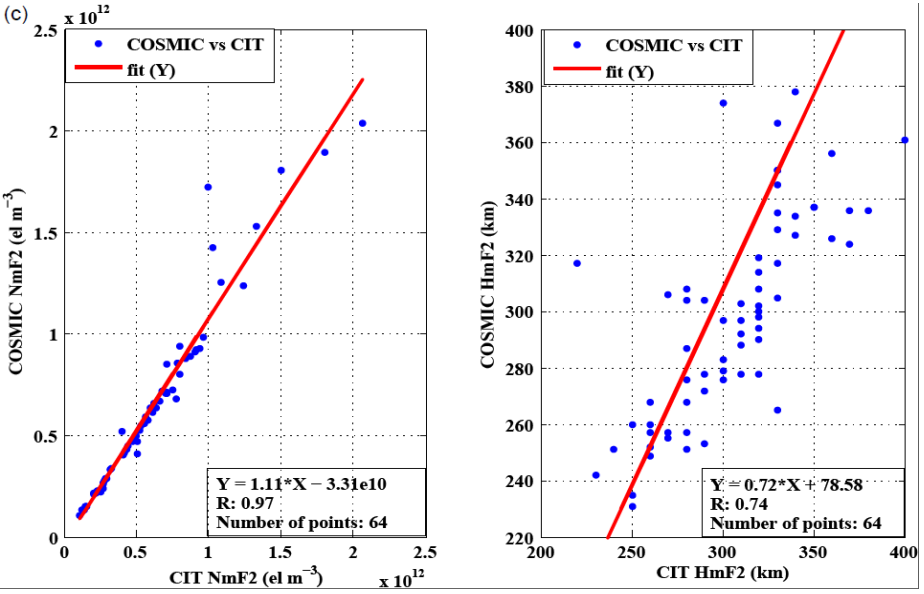

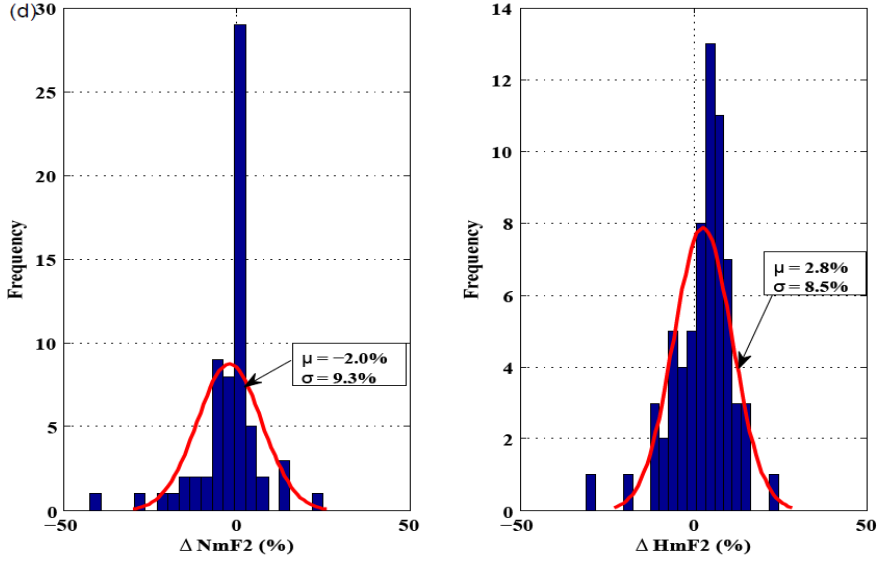

VTEC perturbation component from NICT (ΔTEC)

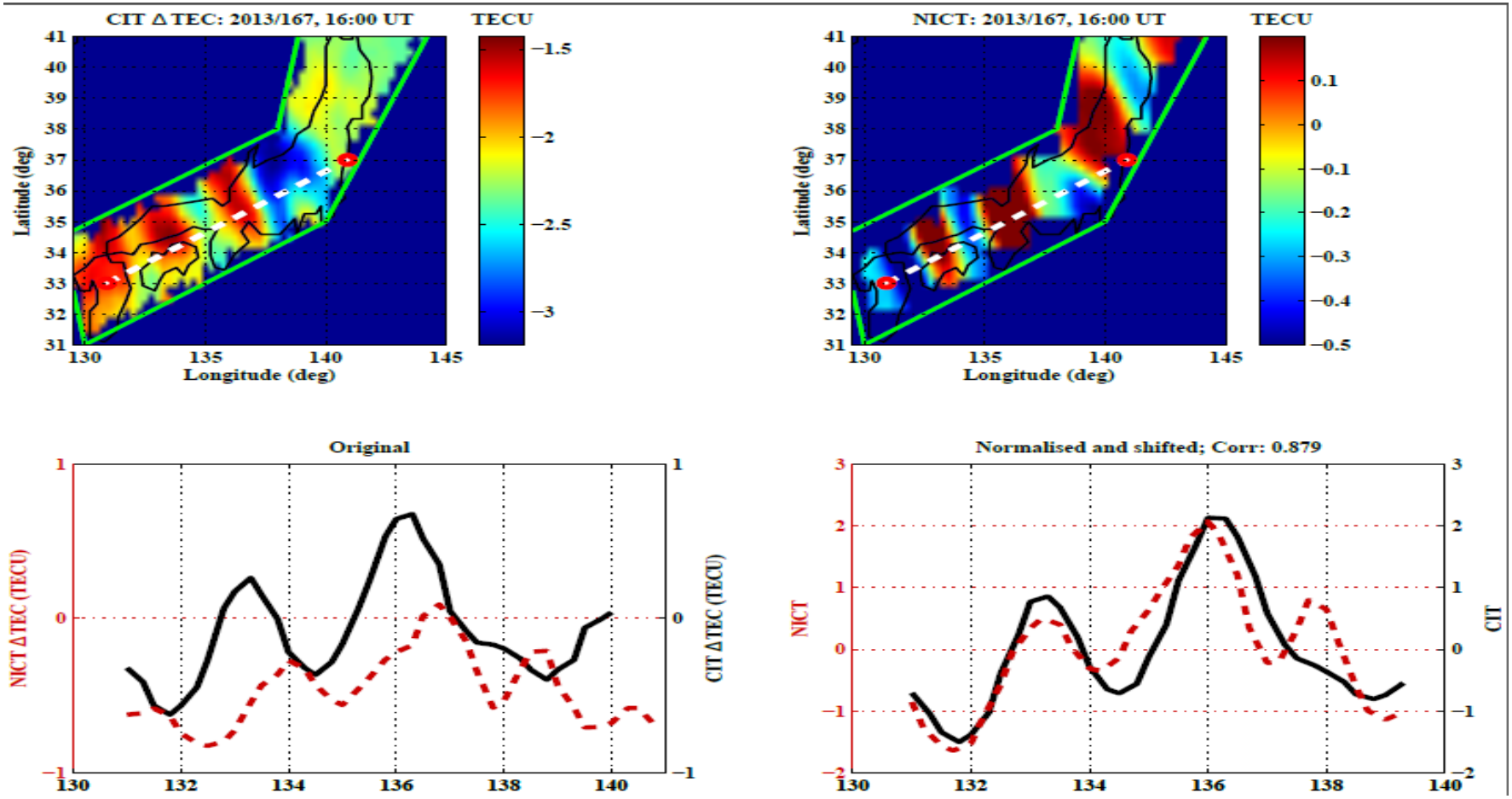

Upper panel: 2D ΔTEC maps of CIT (left) and NICT (right).
Lower panels: horizontal profiles extracted from the 2D ΔTEC maps along the white dashed line. CIT black solid line and NICT red dashed line.
Left lower panel represents the original profiles, while in the **right lower panel** the profiles have been demeaned, normalized by standard deviation and phase difference removed.
Corr represents the correlation coefficient.

Results:

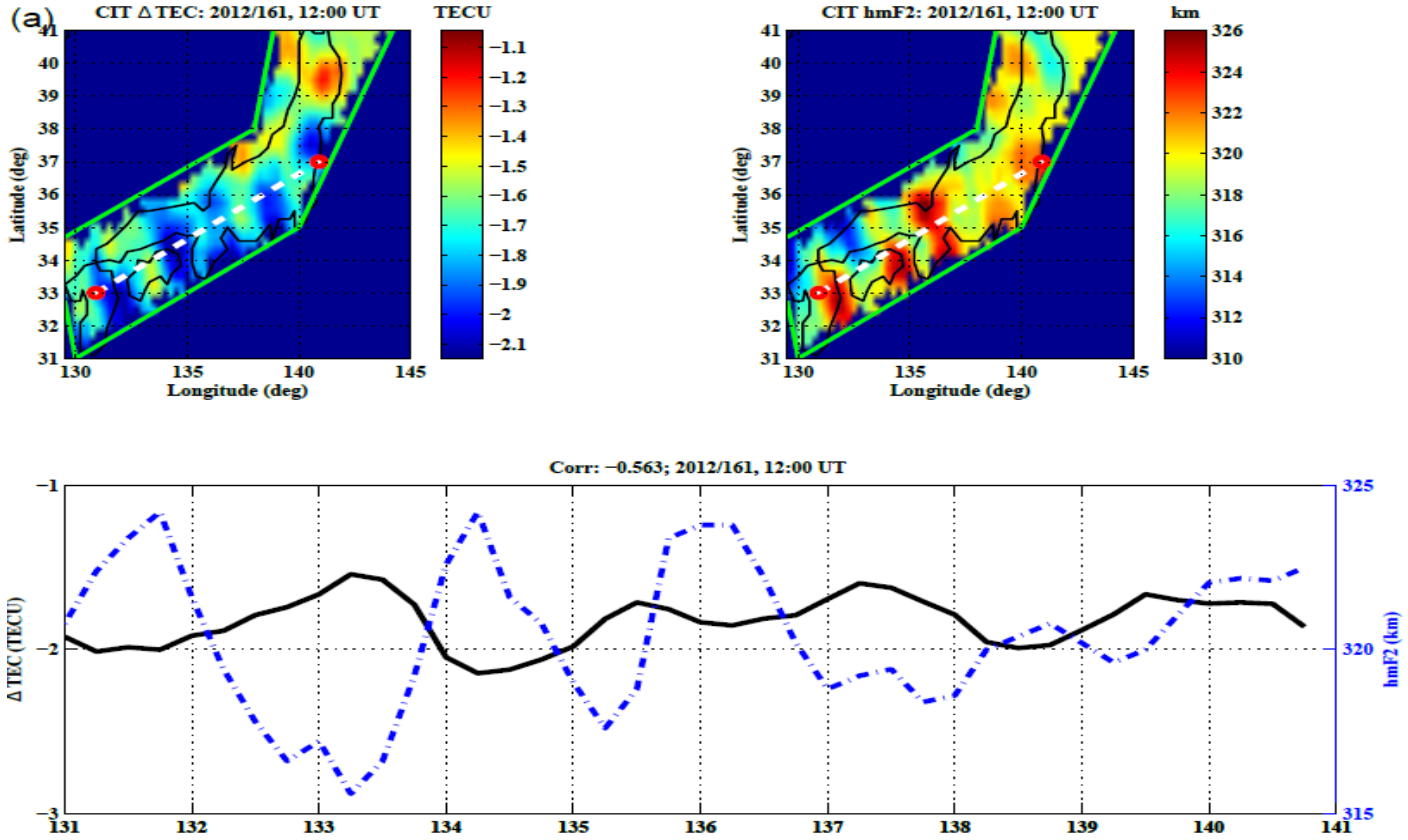

Upper panels: images of CIT ΔTEC and corresponding reconstructed hmF2 at that time stamp shown with the top label.

Lower panels: horizontal profiles extracted from CIT ΔTEC and hmF2 images along the white dashed lines. Solid black and blue dashed doted lines represent ΔTEC and hmF2, respectively.

- The correlation coefficient between the horizontal profiles in each figure was found to be less than -0.5. → Mostly anti-correlates!

Statistical analysis

Table 1: Day of year and period when MSTIDs were present.

2014		2013		2012	
DOY	Time (UT=LT+9)	DOY	Time (UT=LT+9)	DOY	Time (UT=LT+9)
131	10-17	132	11-16	146	10-22
142	10-19	137	10-19	159	10-19
156	10-18	151	11-21	161	10-21
161	10-16	156	11-19	162	11-20
172	13-20	161	10-14		
223	10-18	167	11-20		

- For statistical analysis we have determined the correlation coefficient on 36 horizontal profiles
- In each extracted hmF2 profile we determine the peak-to-peak amplitude (ΔH).
- Only snap shots with more than one peak and ΔH exceeding 10 km were considered.

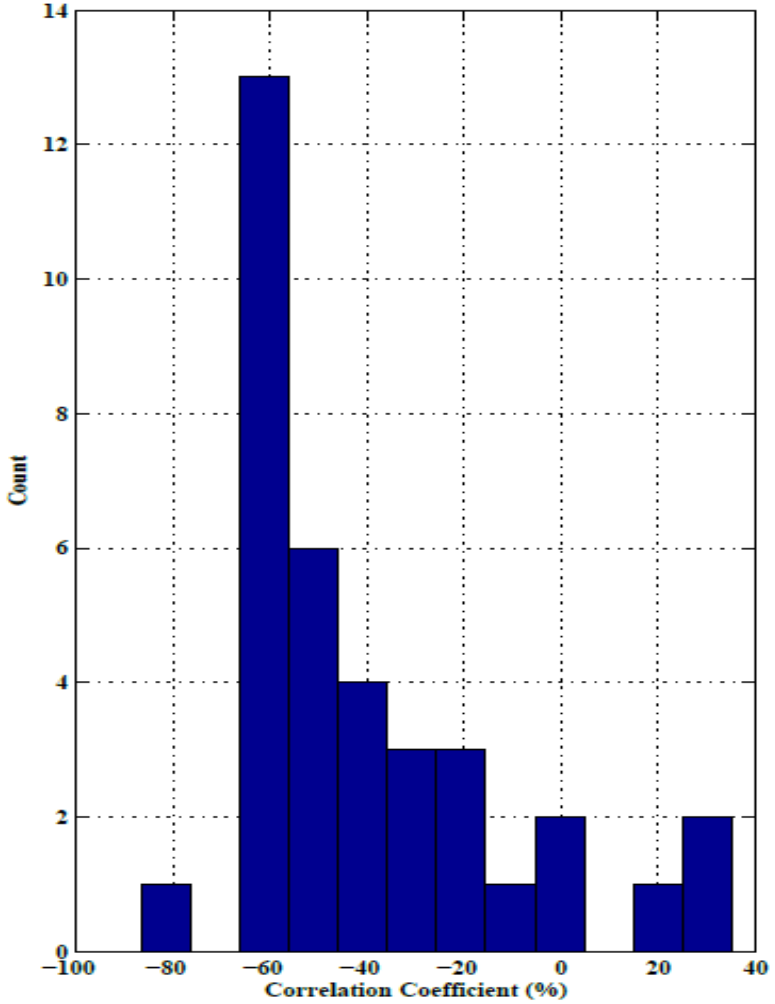

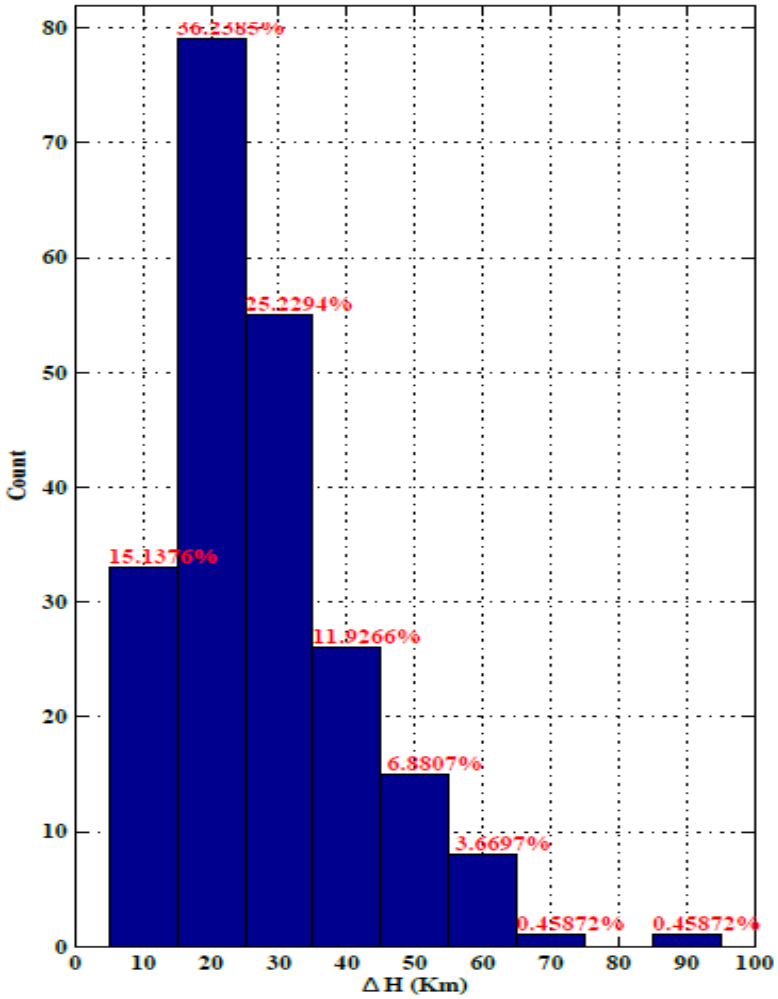

- The dominant correlation coefficient is -60%.
- ΔH has a gamma distribution with dominant amplitudes at 20 km.
- 88% of the amplitudes occur between 10 and 40 km.
- This amplitude is less than the preliminary results reported by Ssessanga et al. (2015).

Conclusion for CIT on MSTID

- We have developed a robust time dependent computerized ionospheric tomography technique, that exhibits a significant substructure in both vertical and horizontal. For the first time we have been able to quantifying the 3D structure of night-time MSTIDs.

- These results agree with previous observations of the nocturnal F layer modulations during MSTIDs.
  - consistent with Behnke [1979]'s ISR observation.
- Results are in agreement with model simulations of night-time MSTIDs (based on an oscillating electric field), which confirms that night-time MSTIDs are driven by electrodynamic forces.
- From the statistical analysis, the F2-peak layer was found to vary in altitude with dominant peak-to-peak amplitudes between 10 and 40 km.

2. Plasmaspheric Tomography

2. Plasmspheric Tomography

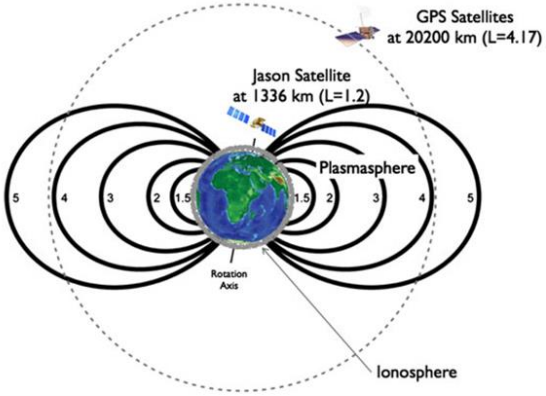

(Lee et al., 2013)

pTEC data from Jason-1

- Indian ($70°\mathrm{E} - 90°\mathrm{E}$), Pacific ($200°\mathrm{E} - 220°\mathrm{E}$), Atlantic ($320°\mathrm{E} - 340°\mathrm{E}$) longitudinal sector
- Periods of high solar ($\mathrm{F10.7} > 100$) and low geomagnetic ($\mathrm{Ap} < 12$) activity
- March, June, September and December from 2002 to 2005

- On average, 1152 ray paths were used for the plasmaspheric tomography for each cases, which cover about 92 percent of the grid for each vertical plane

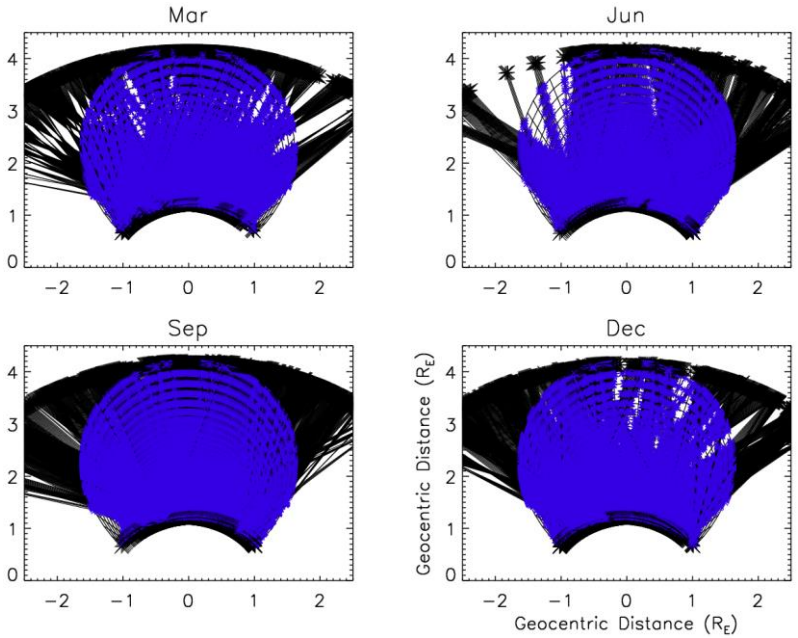

Example of the ray paths during daytime in Indian sector for March, June, September, and December during 2002 – 2005. The black lines are the ray paths and blue symbols represent intersection points between the rays and grid

Reconstructed 2-D plasmasphere

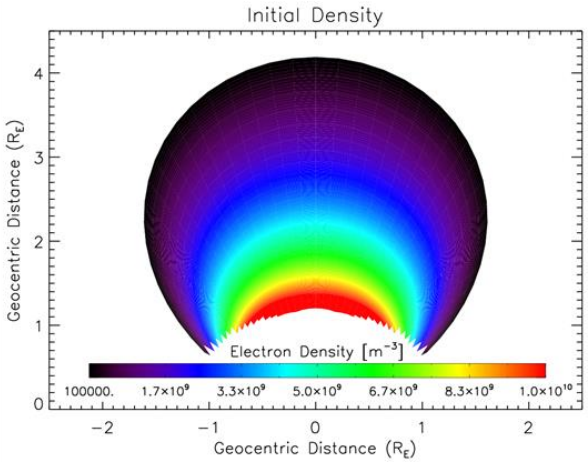

An empirical function of plasmaspheric density along the magnetic field line from Huang et al. (2004)

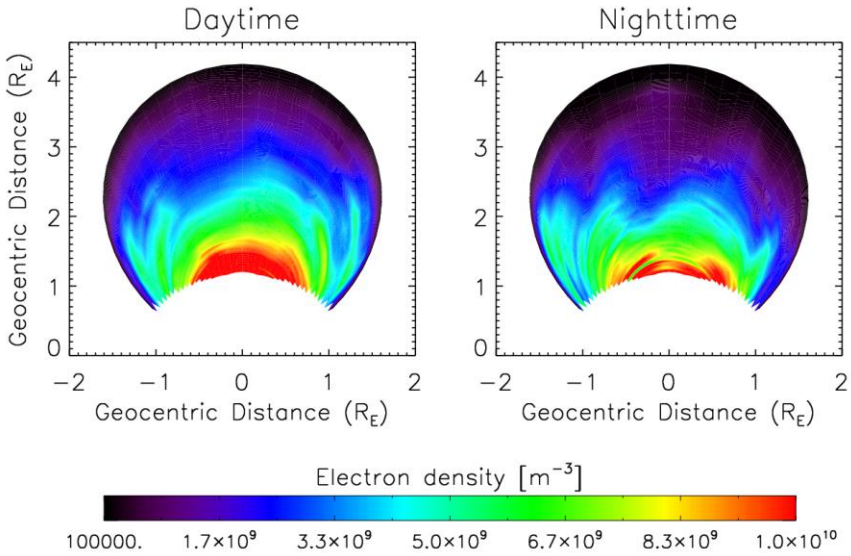

Examples of the tomographic results in Indian sector during daytime (left) and nighttime (right) in June

- The reconstructed density distribution is significantly dissimilar to the field line configuration.

→ Mostly due to the uneven ray path distribution.

→ Some tendency of steeper density gradient on the equatorial plane.

Density profiles on the equatorial plane

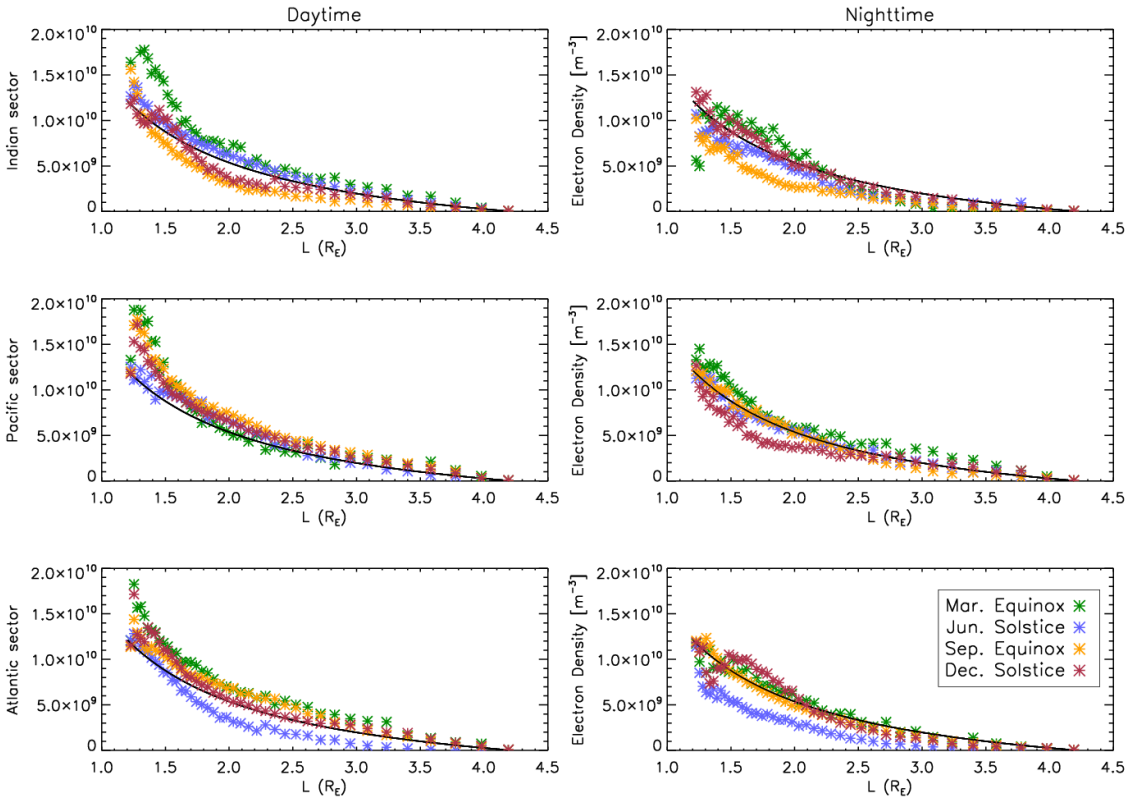

- Mean day to night ratio in the range of $1.2 < L < 4.2 = 1.5$
- The weak diurnal variation of plasmasphere is consistent with previous studies (*e.g., Jayawardena et al., 2015; Lee et al., 2013*)

Density profiles on the equatorial plane

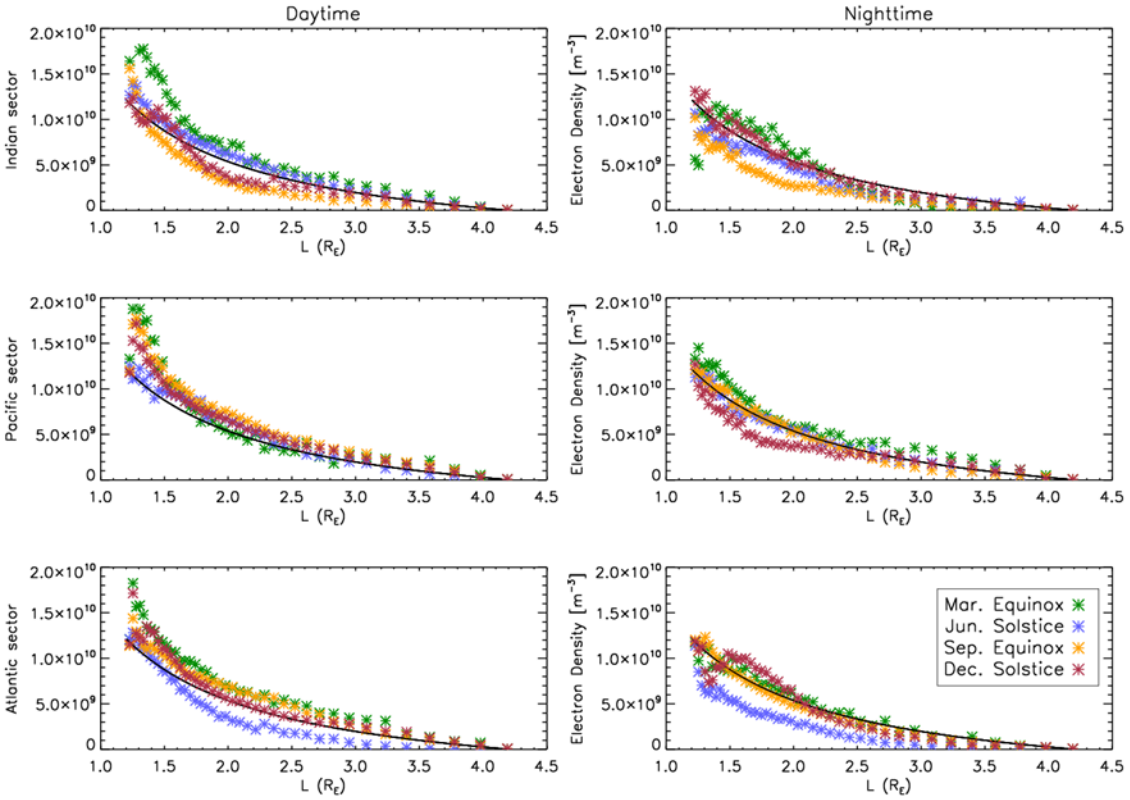

- Atlantic sector : greater in Dec. than in Jun.
- D/J ratio in Atlantic sector : 3.3 (2) during daytime (nighttime)
- However, the annual anomaly is not obvious in Indian and Pacific sector
- This result is consistent with previous studies which observed that the pN_{eq} showed a maximum in Dec. and a minimum in Jun. in a certain longitude sector

Density profiles on the equatorial plane

- We compared our results with an empirical model of the pN_{eq} measured by IMAGE satellite between $2 < \mathrm{L} < 5$ during May 2000 – May 2001 (*Berube et al., 2005*). The least square fit is

$$pN_{eq}(\mathrm{L}) = 10^{-0.66L+4.89}$$

- Our results can be on average given by the expression in the range of $\mathrm{L} = 1.2 - 4.2$:

$$pN_{eq}(\mathrm{L}) = 10^{-0.61L+4.92}$$

- For the first time, we can suggest the empirical functions of pN_{eq} for four seasons in three longitude sectors during daytime and nighttime

Density profiles on the equatorial plane

Longitude	LT	March	June	September	December
Indian	Day	$-0.57L + 5.01$	$-0.57L + 4.90$	$-0.68L + 4.92$	$-0.59L + 4.86$
	Night	$-0.84L + 5.30$	$-0.59L + 4.80$	$-0.67L + 4.82$	$-0.63L + 4.96$
Pacific	Day	$-0.55L + 4.91$	$-0.59L + 4.94$	$-0.55L + 4.95$	$-0.56L + 4.92$
	Night	$-0.50L + 4.80$	$-0.57L + 4.85$	$-0.62L + 4.93$	$-0.51L + 4.65$
Atlantic	Day	$-0.52L + 4.89$	$-0.87L + 5.27$	$-0.55L + 4.89$	$-0.54L + 4.86$
	Night	$-0.59L + 4.89$	$-0.74L + 4.90$	$-0.64L + 4.95$	$-0.66L + 5.01$

- The slopes are mostly slower during daytime than nighttime, indicating that the plasmasphere contracts during nighttime.
- In Pacific and Atlantic sector, the pN_{eq} decreases with increasing L value more rapidly in June than in December, implying that the plasmaspheric density might be smaller in June than in December.

Conclusion for Plasmaspheric Tomography

- We developed a plasmaspheric tomography algorithm using the Jason pTEC data.
- The reconstructed plasmaspheric density distribution reasonably well displays the general characteristics of the plasmasphere, which is mostly consistent with previous studies (*e.g. Clilverd et al., 2007; Lee et al., 2013*)
  - Weak diurnal variations (daytime > nighttime) by a factor of 1.5
  - Annual anomaly (December > June) in the Atlantic sector
- We estimated the empirical functions of the pN_{eq} for each case.
- The direct observations of the global density distribution of the plasmasphere is insufficient.

→ The plasmaspheric tomography using plasmaspheric TEC data can provide the global density distribution of the plasmasphere.

THANKS

4 D VAR SLIDES

Rocket trajectory

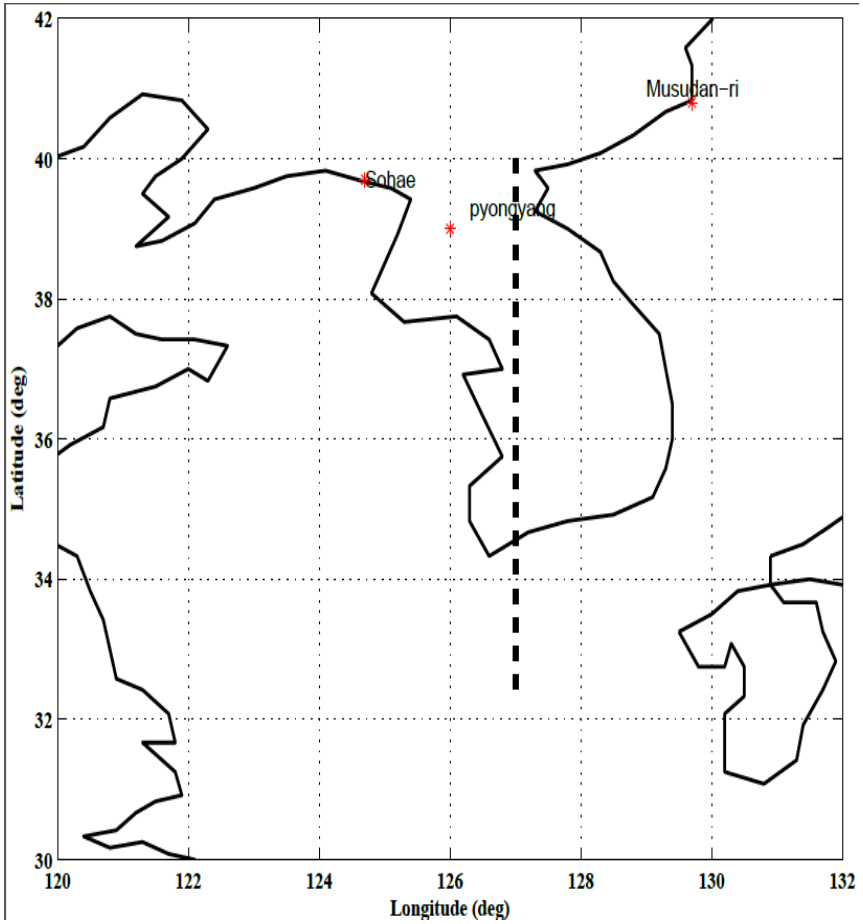

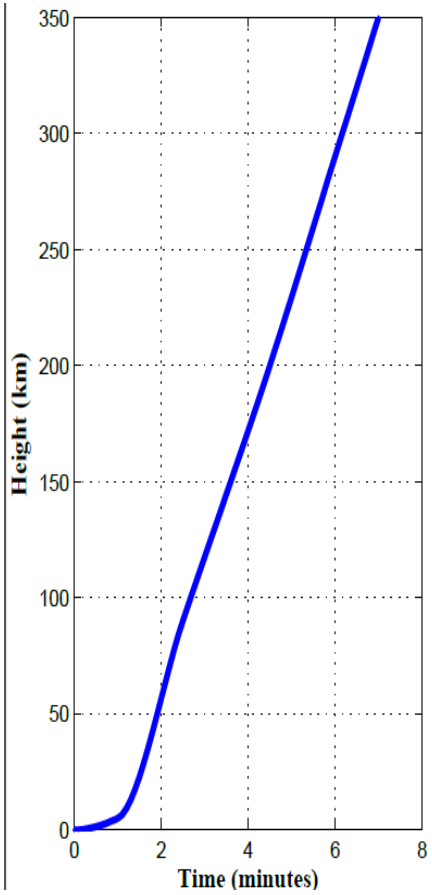

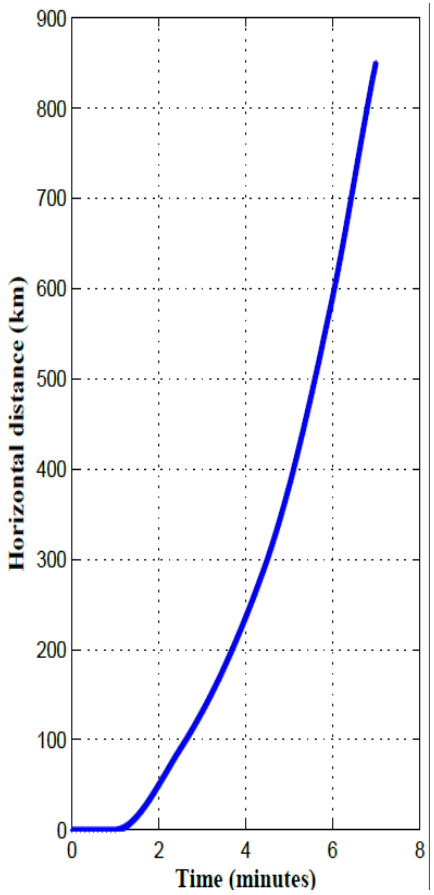

Trajectory values assumed from: Ionospheric hole made by ballistic missile from North Korea (Masaru Ozeki and Kosuke Heki)

Water model and Ionospheric hole after rocket launch

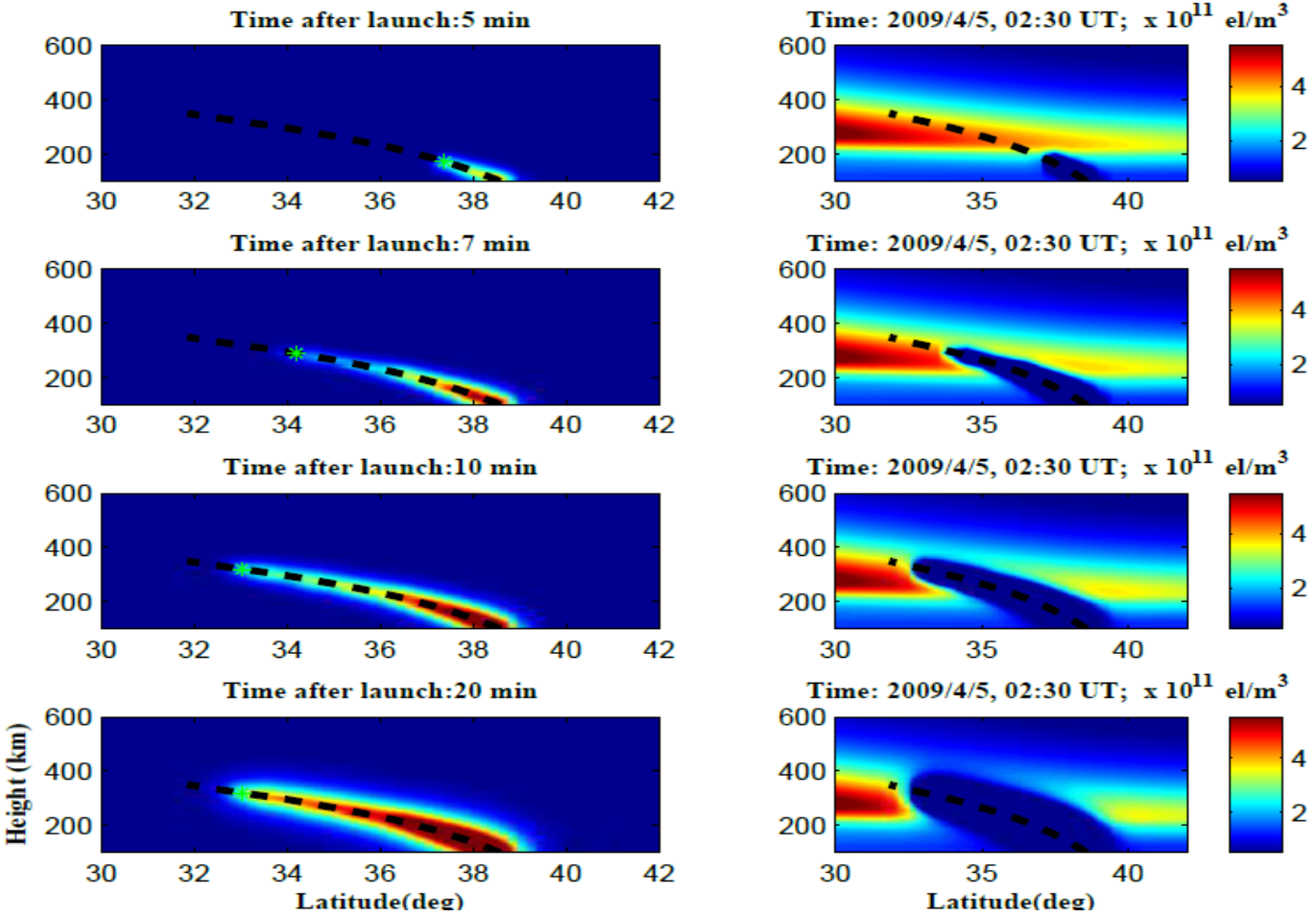

Left panel: water diffusion model using emission of 8.5 x10^{28} s-1.
Right panel: Ionospheric hole after launch.

Change in STEC due Rocket launch

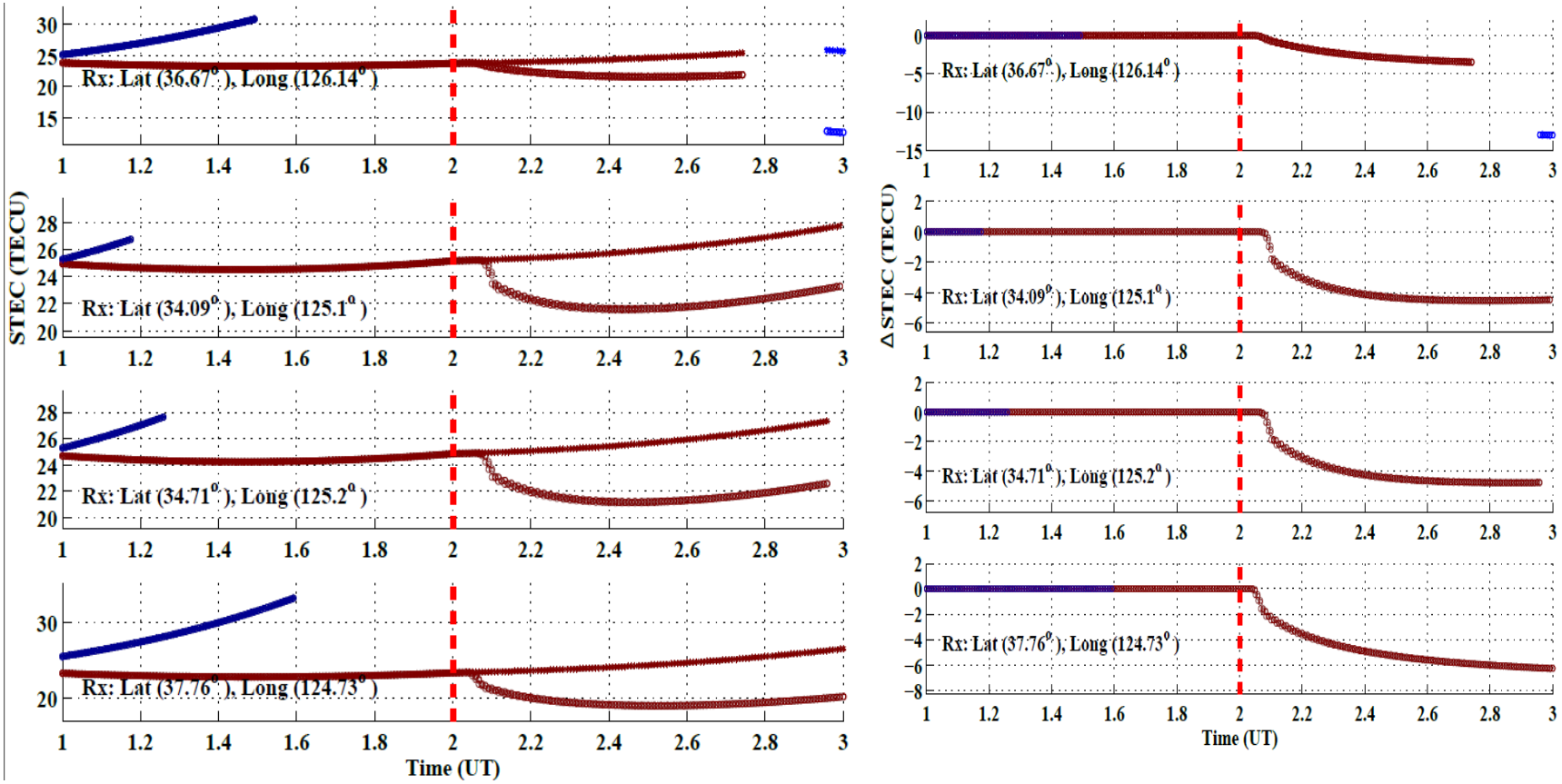

Left panel: Change in STEC due to Rocket launch.
Right panel: Delta STEC (original – New STEC after launch)

Cost function

$$J(X,E) = \frac{1}{2}\left[(E-E_b)^T Q^{-1}(E-E_b)^T + (X-X_b)^T B^{-1}(X-X_b)\right]$$

$$+\frac{1}{2}\left[\sum_{k=0}^{k=N}(H_k X_k - Y_k)^T R^{-1}(H_k X_k - Y_k)\right]$$

E - Emissions;

E_b- Background emissions

Q - Error covariance matrix of emissions

X - Electron density.

X_b- Background electron density from IRI.

B - Error covariance matrix of background electron density

k - Time

H_k - Design matrix at time k

X_k - Estimated electron density at time k

Y_k - Measurements (STEC) at time k

Optimization using Lagrange multiplier method

$$\lambda^N = H_N^T R_N^{-1}(H_N X_N - Y_N)$$

$$\lambda^k = \left(\frac{\partial X_{k+1}}{\partial X_k}\right)^T \lambda^{k+1} + H_k^T R_k^{-1}(H_k X_k - Y_k)$$

$$E = E_b - Q\sum_{k=0}^{N-1}\left(\frac{\partial X_{k+1}}{\partial E_k}\right)^T \lambda^{k+1}$$

$$X = X_b - B\lambda^0$$

Results

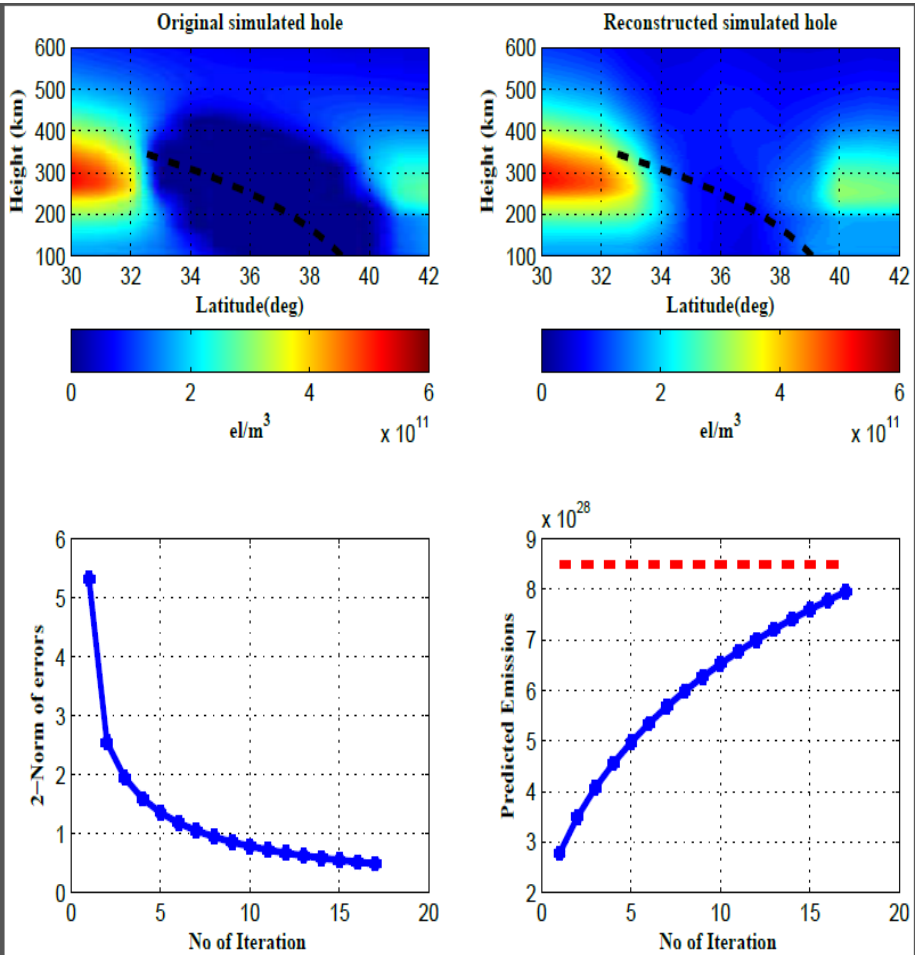
Original simulated hole
Reconstructed simulated hole
Height (km)
Latitude(deg)
el/m3
x 10^11
2−Norm of errors
No of Iteration
Predicted Emissions
x 10^28

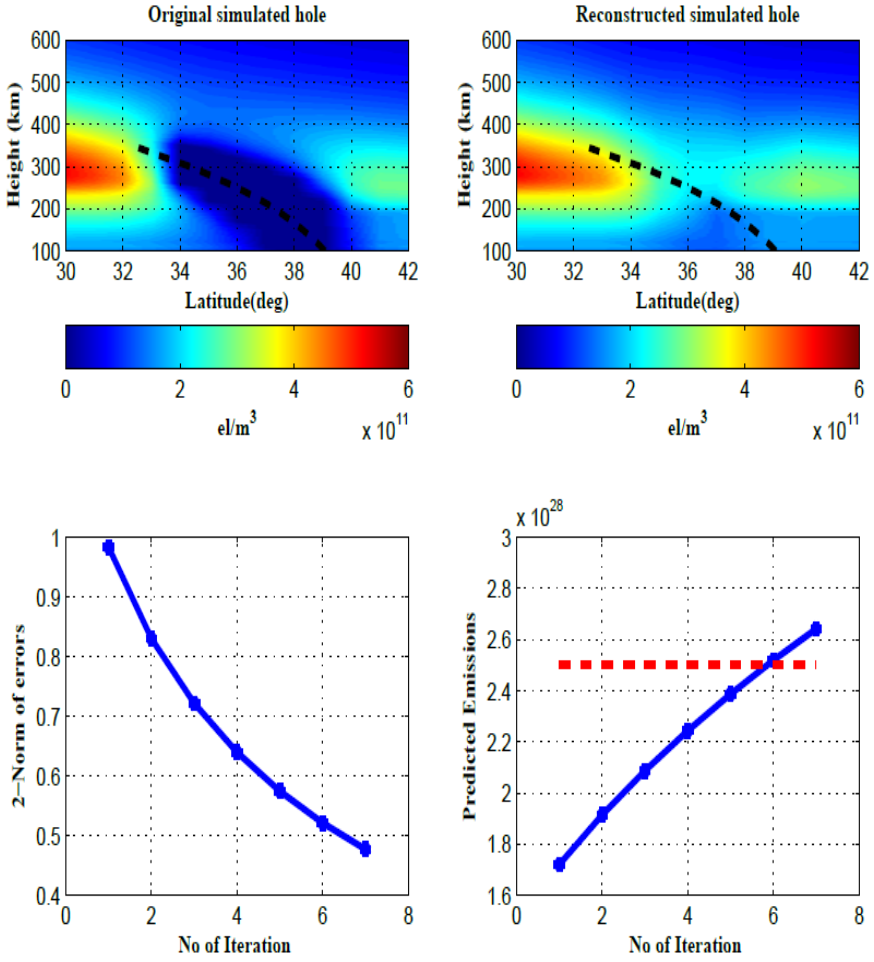
Original simulated hole
Reconstructed simulated hole
Height (km)
Latitude(deg)
el/m3
x 10^11
2−Norm of errors
No of Iteration
Predicted Emissions
x 10^28

Predicted emissions

Original x 1e28 s^{-1}	Initial guess x 1e28 s^{-1}	Final x 1e28 s^{-1}	Error(difference) x 1e28 s^{-1}
8.5	1.5	7.9519	0.5481
6.5	1.5	6.5586	-0.0586
4.5	1.5	4.9128	-0.4128
2.5	1.5	2.6417	-0.1417